Article

Nano-Crystallization of Ln-Fluoride Crystals in Glass-Ceramics via Inducing of Yb^{3+} for Efficient Near-Infrared Upconversion Luminescence of Tm^{3+}

Jianfeng Li, Yi Long, Qichao Zhao, Shupei Zheng *, Zaijin Fang * and Bai-Ou Guan

Guangdong Provincial Key Laboratory of Optical Fiber Sensing and Communications,
Institute of Photonics Technology, Jinan University, Guangzhou 511443, China; ljf151@stu2019.jnu.edu.cn (J.L.);
longyi9604@stu2019.jnu.edu.cn (Y.L.); a1290816237@stu2020.jnu.edu.cn (Q.Z.); tguanbo@jnu.edu.cn (B.-O.G.)
* Correspondence: spzheng@jnu.edu.cn (S.Z.); fzj909@jnu.edu.cn (Z.F.)

Abstract: Transparent glass-ceramic composites embedded with Ln-fluoride nanocrystals are prepared in this work to enhance the upconversion luminescence of Tm^{3+}. The crystalline phases, microstructures, and photoluminescence properties of samples are carefully investigated. KYb$_3$F$_{10}$ nanocrystals are proved to controllably precipitate in the glass-ceramics via the inducing of Yb^{3+} when the doping concentration varies from 0.5 to 1.5 mol%. Pure near-infrared upconversion emissions are observed and the emission intensities are enhanced in the glass-ceramics as compared to in the precursor glass due to the incorporation of Tm^{3+} into the KYb$_3$F$_{10}$ crystal structures via substitutions for Yb^{3+}. Furthermore, KYb$_2$F$_7$ crystals are also nano-crystallized in the glass-ceramics when the Yb^{3+} concentration exceeds 2.0 mol%. The upconversion emission intensity of Tm^{3+} is further enhanced by seven times as Tm^{3+} enters the lattice sites of pure KYb$_2$F$_7$ nanocrystals. The designed glass ceramics provide efficient gain materials for optical applications in the biological transmission window. Moreover, the controllable nano-crystallization strategy induced by Yb^{3+} opens a new way for engineering a wide range of functional nanomaterials with effective incorporation of Ln^{3+} ions into fluoride crystal structures.

Keywords: nano-crystallized glass ceramic; nano-crystallization; luminescence; Tm^{3+} doped; upconversion

1. Introduction

Trivalent lanthanide (Ln^{3+}) ions doped upconversion (UC) luminescent materials have been extensively investigated for applications in lighting, solar cells, solid-state laser, biological imaging, and temperature sensing due to the multiple luminescence wavelength from ultraviolet to near-infrared (NIR) regions [1–9]. Among these, Tm^{3+} doped materials possess UC luminescence in the NIR region at around 800 nm ($^3H_4 \rightarrow ^3H_6$), which is located in the biological transmission window, and the light in that region can easily penetrate biological tissues [10–13]. Moreover, the UC emissions of Tm^{3+} are dramatically enhanced via the energy transfer (ET) from Yb^{3+}, which possesses a large absorption section for the commercial 980 nm lasers. Thus, Yb^{3+}-Tm^{3+} co-doped materials were more efficient candidates for NIR-to-NIR UC luminescence and were significant light sources for biologically non-destructive detection. In the past decades, a large number of investigations about Yb^{3+}-Tm^{3+} co-doped UC materials have been widely reported for achieving high-efficiency NIR UC luminescence [14–20].

Glass exhibits high transmittance, easy fabrication, and excellent processability due to its amorphous and softening characteristics. These properties make glass an appealing matrix for the design and fabrication of special optics devices, particularly of optical fiber lasers [21,22], which can hardly be achieved by using crystals. Furthermore, nano-crystallized glass ceramic (GC) composites can be obtained via the precipitation of

functional nanocrystals in a glass matrix via heat treatments. The nano-crystallized GCs still possess high optical transmittance and the UC luminescence efficiency in GCs can be greatly enhanced, as compared to glass, when Ln^{3+} ions are successfully incorporated into the crystal structures featuring lower probability of non-radiative transition ascribed to the lower phonon energy. So far, Yb^{3+}-Tm^{3+} co-doped GCs have been considered as significantly optical gain materials for UC NIR fiber lasers, noncontact optical thermometers, and bio-imaging [23–26]. Generally, Ln^{3+} ions were expected to incorporate into the crystal structures via the ionic substitution for Y^{3+}, La^{3+}, Lu^{3+}, Sc^{3+}, and Sr^{2+} in the GCs embedded with $Na(Y/La/Lu)F_4$, LaF_3, YF_3, KSc_2F_7, and SrF_2 crystals, etc [27–31]. However, the ionic substitution process was uncontrollable and the amount of Ln^{3+} incorporated into the crystal structures was usually small due to the large mismatch between Ln^{3+} and the replaceable sites. The enhancements of luminescence in GCs were limited. Moreover, a lot of remaining crystals not occupied by Ln^{3+} ions made no contribution to the enhancement of luminescence but will trigger severe issues of optical scattering and low optical transmittance in glass. These made the traditional GCs difficult to be used in the practical applications. Accordingly, it is highly desirable for design and fabrication of novel GCs for controllably incorporating a large number of Ln^{3+} into crystal structures to achieve high-efficiency NIR UC luminescence of Tm^{3+}.

Ln-fluoride crystal, intrinsically containing Ln^{3+} (for example, Yb^{3+} or Er^{3+}) in the crystal lattices, is a significant host for the incorporation of other active Ln^{3+} ions because the mismatches in ionic radius between different Ln^{3+} ions are smaller and active Ln^{3+} ions enter Ln-fluoride crystals more easily [32]. In this work, GCs containing Ln-fluoride nanocrystals were designed to greatly enhance the UC luminescence of Tm^{3+} and achieve pure, high-efficiency NIR-to-NIR emissions. Two kinds of Ln-fluoride nanocrystals (KYb_3F_{10} and KYb_2F_7) were controllably precipitated from a glass matrix via the heat treatments dependent on the doping of Yb^{3+}. Tm^{3+} ions entered the fluoride crystal lattices easily by replacing Yb^{3+} sites. As a result, a large number of Ln^{3+} were incorporated into the fluoride crystals featuring extremely low phonon energy and the UC emission of Tm^{3+} in the GCs were dramatically enhanced. Moreover, the pure NIR UC emissions were also obtained by adjusting the doping concentration of Tm^{3+}. Thus, the designed GCs provide an efficient material for pure NIR UC luminescence and offer highly promising developments for UC fiber lasers, non-contact optical thermometers, and bio-imaging.

2. Materials and Methods

2.1. Materials Preparation

Samples with a molar composition of $70SiO_2$-$15KF$-$15ZnF_2$-$xYbF_3$-yTm_2O_3 ($x = 0{\sim}3.5$, $y = 0{\sim}0.3$) were prepared using a melt quenching method. First, 30 g reagent grade stoichiometric mixtures were mixed thoroughly in an agate mortar and melted in covered quartz crucibles in an electric furnace at 1550 °C for 30 min; the melts were poured onto a brass plate and then pressed using another brass plate to obtain precursor glasses (PGs). PG samples were heated at 540 °C for 5 and 10 h to obtain GC samples according to the differential scanning calorimetry (DSC) results in ref. [33]. PG and GC samples were cut and polished to 2 mm thick for measurements.

2.2. Characterizations

To identify the crystalline phase in GCs, X-ray diffraction (XRD) patterns were performed on a X-ray diffractometer (Bruker, Fällanden, Switzerland) with Cu/Ka ($\lambda = 0.1541$ nm) radiation. The morphology and size distribution of the nanocrystals in GCs were measured via high-resolution transmission electron microscopy (HRTEM) (FEI, Hillsboro, OR, USA). UC emission spectra of samples were recorded using an Edinburgh FLS980 fluorescence spectrometer (Edinburgh Instruments, Edinburgh, UK). A 980 nm laser diode (LD) was used as the exciting source for the measurement of UC emission spectra. The emission decay curves were measured using the same spectrometer with a microsecond lamp as the excitation source. All measurements were performed at room temperature.

3. Results and Discussion

Figure 1a shows the XRD patterns of Yb^{3+}-Tm^{3+} co-doped PG and GCs. A broad band is observed in the XRD pattern of PG due to the amorphous characteristic of glass. Sharp peaks are observed in the XRD patterns of the two GCs. The main peaks at 26.99°, 31.27°, 44.81°, and 53.1° are ascribed to the (222), (400), (440), and (622) crystal facets of KYb_3F_{10} (No: 74-2204), respectively, indicating that KYb_3F_{10} crystals have been precipitated in the GCs. Moreover, weak peaks at 18.86°, 31.04°, and 38.28° attributed to the diffraction peaks of K_2SiF_6 (No: 85-1382) crystals are also observed in the XRD patterns of GC heated at 540 °C for 5 h. It is also found that the intensities of diffraction peaks for KYb_3F_{10} crystal are all increased when the heating time increases from 5 to 10 h. However, the diffraction peaks of K_2SiF_6 crystal all weaken due to the further heat treatment to 10 h. These results indicate that KYb_3F_{10} crystals prefer to precipitate in the 1.0Yb^{3+}-0.005Tm^{3+} co-doped GCs via the further heat treatment. Additionally, the average size of crystals can be calculated by the Scherrer's equation. The diffraction peak, around 2θ = 27.01° and 18.42°, was selected for the calculation, and the average size of the KYb_3F_{10} and K_2SiF_6 nanocrystals in the GC heated at 540 °C for 5 h was calculated to be approximately 13.35 and 31.34 nm, respectively.
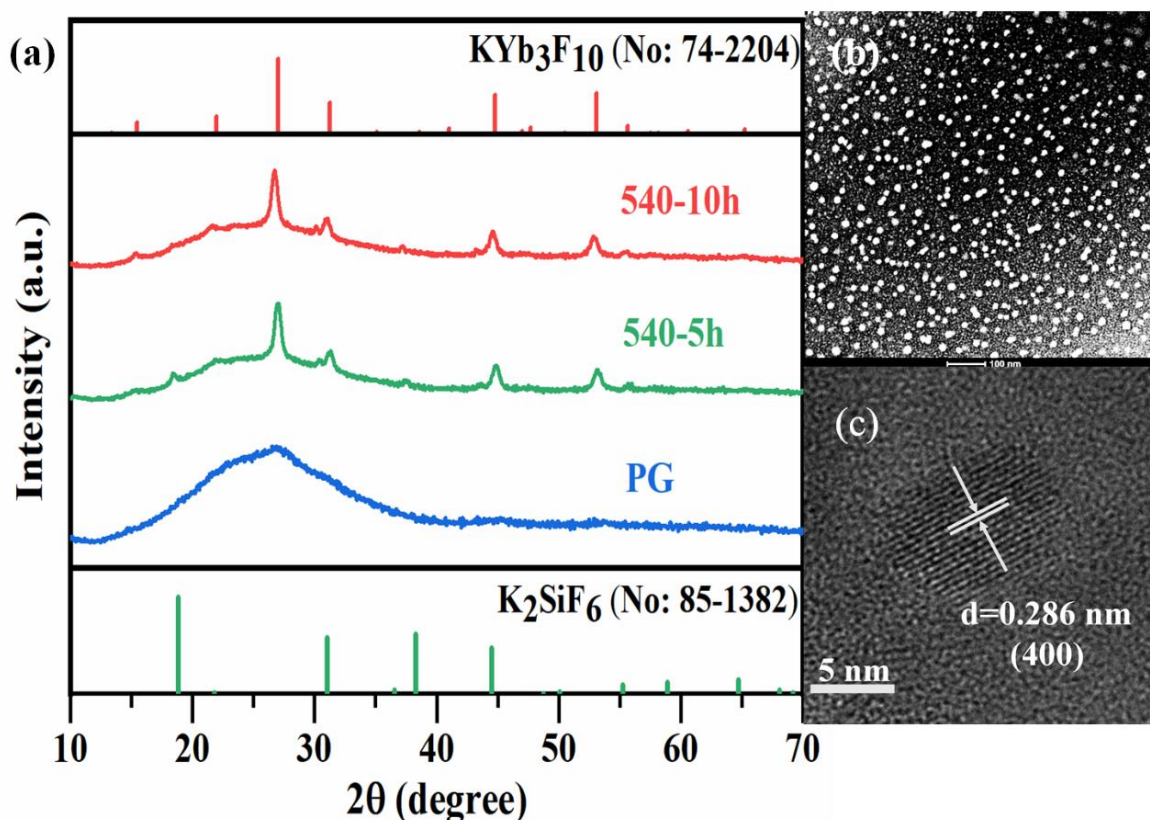
Figure 1. (**a**) XRD patterns of 1.0Yb^{3+}-0.005Tm^{3+} co-doped PG and GCs. (**b**) TEM and (**c**) HRTEM images of 1.5Yb^{3+}-0.1Tm^{3+} co-doped GC heat treated at 540 °C for 10 h.

The HAADF-TEM image shown in Figure 1b reveals that the nanocrystals are in-situ, precipitated among the glass matrix. The measured size of these nanoparticles is from 10 to 30 nm. The HR-TEM image is shown in Figure 1c. The crystal lattice fringes are obvious, which is different from that of the amorphous glass matrix. The interval of the crystal lattice fringes d can be measured directly, and its value is about 0.286 nm, which corresponds to the (400) crystal facet of cubic KYb_3F_{10}. These also prove that KYb_3F_{10} nanocrystals are precipitated in the GCs.

The optical transmission spectra of the $1.0Yb^{3+}$-$0.1Tm^{3+}$ co-doped samples are shown in Figure 2a. The PG sample possesses high transmittance (~90%) from 300 to 800 nm with a thickness of 2 mm. Though nanocrystals are precipitated in the GCs, the optical transmittances of GCs are still as high as 85%. Interestingly, the transmittance of the GC heated for 10 h is higher than that heated for 5 h. As calculated from the XRD patterns, the average size of KYb_3F_{10} crystals is smaller than that of K_2SiF_6 crystals. When the heat treatment time increases from 5 to 10 h, more KYb_3F_{10} crystals and less K_2SiF_6 crystals are precipitated in the GC, resulting in the increase of transmittance.
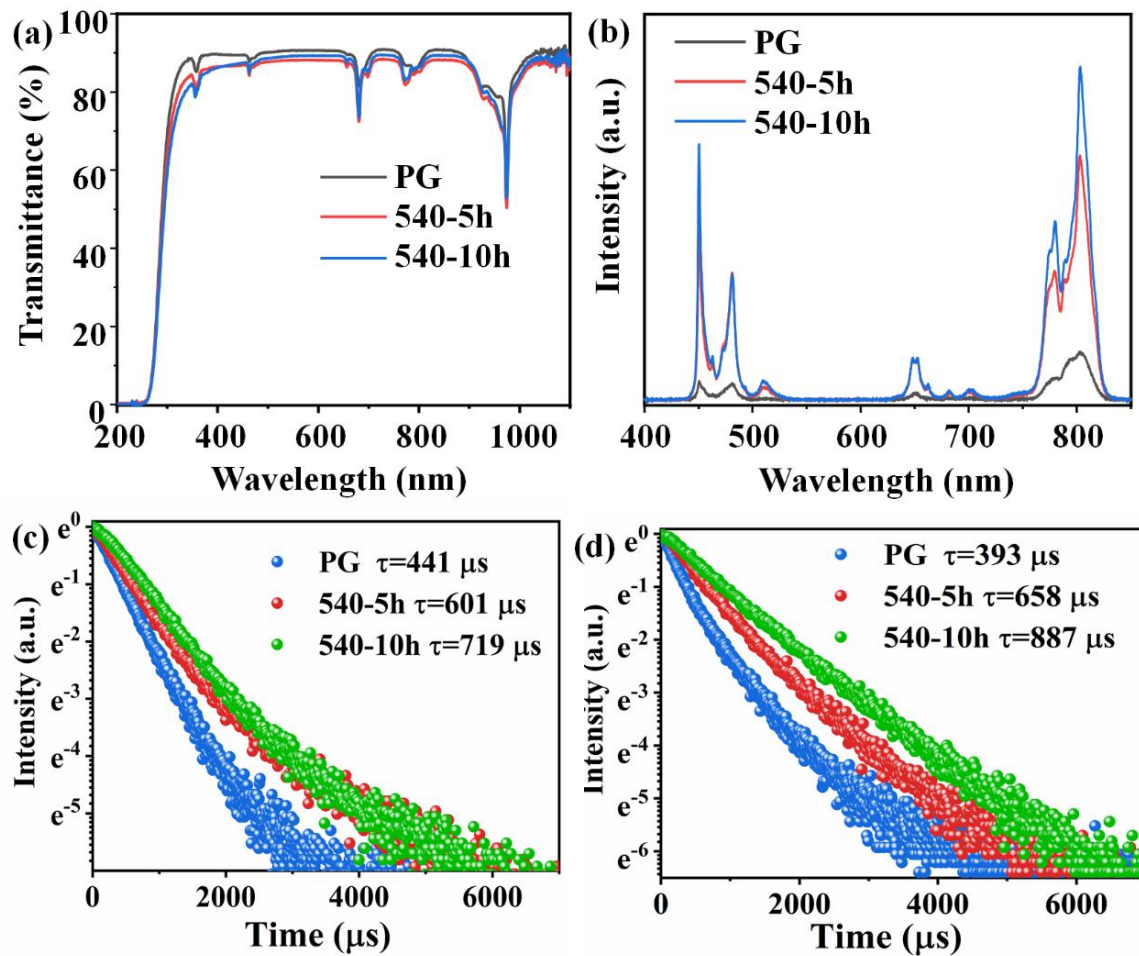
**Figure 2.** (**a**) Transmission spectra of $1.0Yb^{3+}$-0.1Tm co-doped PG and GC. (**b**) UC emission spectra $1.0Yb^{3+}$-$0.005Tm^{3+}$ co-doped PG and GCs. (**c**) Emission decay curves of $1.0Yb^{3+}$-$0.005Tm^{3+}$ co-doped PG and GCs monitored at 450 nm emission. (**d**) Emission decay curves of $1.0Yb^{3+}$-$0.005Tm^{3+}$ co-doped PG and GCs monitored at 802 nm emission.

Figure 2b shows the emission spectra of $1.0Yb^{3+}$-$0.005Tm^{3+}$ co-doped PG and GCs recorded at room temperature upon the excitation of a 980 nm laser diode (LD). The spectra all include a NIR emission peak at 802 nm attributed to the $^3H_4 \rightarrow {}^3H_6$ transition of Tm^{3+}. Meanwhile, the blue (450 and 480 nm), red (650 nm), and deep red emission peaks (680 and 700 nm) attributed to $^1D_2 \rightarrow {}^3F_4$, $^1G_4 \rightarrow {}^3H_6$, $^1G_4 \rightarrow {}^3F_4$, $^3F_2 \rightarrow {}^3H_4$, and $^3F_3 \rightarrow {}^3H_4$ transition of Tm^{3+} [34,35], respectively, are all observed in the emission spectra of PG and GC samples. Since Tm^{3+} exhibits no absorption for 980 nm light, these emissions are all obtained via the ET processes from Yb^{3+} to Tm^{3+}. In addition, the emission peaks of GCs are narrower than that of PG and the splitting of spectrum by crystal fields are observed in the spectra of GCs, indicating the incorporation of Tm^{3+} into crystal coordinated sites. It is also found from the spectra that the emission intensity at 450 and 802 nm increases 15 and 6 times after the heat treatment for 10 h, respectively. Figure 2c,d show the emission decay curves monitored at

450 and 802 nm, respectively. The emission lifetime at 450 nm increases from 441 to 601 and 719 μs, and that at 802 nm increases from 393 to 658 and 887 μs when the sample is heated at 540 °C for 5 and 10 h, respectively. These results are attributed to the fact that the low phonon energy environment reduces the possibility of non-radiative transition and enhances the emission intensity and lifetime in the sample, which in turn prove the incorporation of Tm^{3+} into the fluoride nanocrystals in GCs. Actually, it is difficult for Tm^{3+} to enter K_2SiF_6 crystal structures due to the lack of appropriate sites for the substitution of Tm^{3+}. However, Tm^{3+} can easily incorporate into KYb_3F_{10} crystal structures by occupying the sites of Yb^{3+} because the ionic radiuses of Tm^{3+} (R = 0.086 nm) and Yb^{3+} (R = 0.085 nm) are very similar. Accordingly, the incorporation of Tm^{3+} into KYb_3F_{10} nanocrystals is responsible for the enhancements of emission intensities and lifetimes in GCs.

The double-logarithmic plots of the excitation power dependency on the emission intensities are presented in Figure 3a. The fitted slope (n) of the plot of Ln (I_{UC}) versus Ln (Power) is used to determine the absorbed photon numbers per UC emitted [36,37]. The obtained value of n was 1.67, 1.73, 2.67, and 3.40 corresponding to the 802, 700, 650, and 450 nm emission of $1.0Yb^{3+}$-$0.005Tm^{3+}$ co-doped GC, respectively. These prove that the emissions are all attributed to UC emission of Tm^{3+} and obtained via the ET from Yb^{3+}. Two, two, three, and four pump photons are needed to pump the electrons to $^3H_4$, $^3F_{2,3}$, $^1G_4$, and $^1D_2$ energy levels of Tm^{3+} to achieve the corresponding UC emissions, respectively.
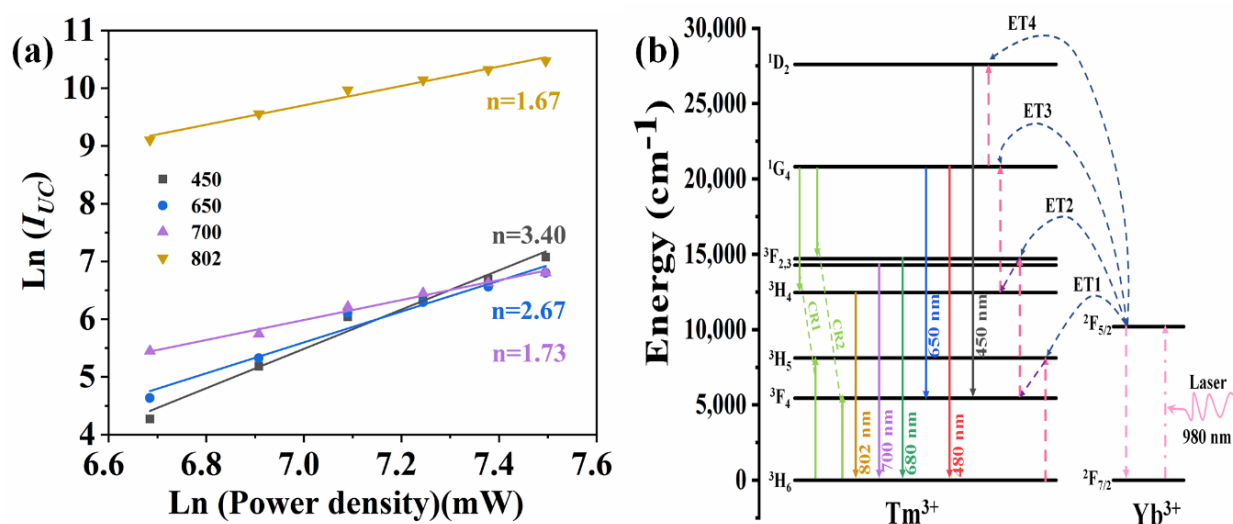
Figure 3. (**a**) Ln-Ln plots of UC emission intensity versus excited power density of 980 nm laser. (**b**) Schematic diagrams of energy levels and relative transitions in KYb_3F_{10}:Tm^{3+} GCs.

Based on these, the energy levels of Tm^{3+} and Yb^{3+} and the relative transitions corresponding to the above UC emissions are illuminated in Figure 3b [38–40]. Under 980 nm LD excitation, the electrons of Yb^{3+} are excited from the ground state $^2F_{7/2}$ to the $^2F_{5/2}$ excited state, then the energy is transferred to Tm^{3+} through the ET1 process: [$^2F_{5/2}$ (Yb^{3+}) + $^3H_6$ (Tm^{3+})→$^2F_{7/2}$ (Yb^{3+}) + $^3H_5$ (Tm^{3+}) + phonons]. The electrons of Tm^{3+} are excited from the ground state to the $^3H_5$ excited state and then undergo a non-radiative relaxation transition to the $^3F_4$ energy level. Via the ET2 process, [$^2F_{5/2}$ (Yb^{3+}) + $^3F_4$ (Tm^{3+})→$^2F_{7/2}$ (Yb^{3+}) + $^3F_{2,3}$ (Tm^{3+}) + phonons], the electrons are populated to the $^3F_{2,3}$ energy level. A part of the electrons undergo a non-radiative relaxation transition to $^3H_4$ energy level. In this process, $^3H_4$→$^3H_6$ (802 nm) and $^3F_{2,3}$→$^3H_6$ (700 and 680 nm) transitions are obtained. Next, part of the electrons at $^3H_4$ energy levels are excited to $^1G_4$ energy through the process of ET3: [$^2F_{5/2}$ (Yb^{3+}) + $^3H_4$ (Tm^{3+})→$^2F_{7/2}$ (Yb^{3+}) + $^1G_4$ (Tm^{3+}) + phonons]. This produces $^1G_4$→$^3H_6$ (480 nm) and $^1G_4$→$^3F_4$ (650 nm) transitions. Finally, the electrons of the $^1G_4$ energy level are populated to the $^1D_2$ energy level through

the process of ET4, [$^2F_{5/2}$ (Yb^{3+}) + $^1G_4$ (Tm^{3+})→$^2F_{7/2}$ (Yb^{3+}) + $^1D_2$ (Tm^{3+}) + phonons], producing a $^1D_2$→$^3F_4$ (450 nm) transition.

Furthermore, the transitions of Tm^{3+} are also modulated via the interaction between neighboring Tm^{3+} ions, which is directly determined by the doping concentration of Tm^{3+} ions [41,42]. The dependence of UC emission spectrum on the doping concentration of Tm^{3+} in the co-doped PG and GC is presented in Figure 4a,b. It can be observed from the spectra that the blue emission intensities at 450 nm and 480 nm both decrease monotonically with the increase of Tm^{3+} concentration, while the NIR emission intensity at 802 nm experiences first an enhancement and then a decrease due to the further increase of Tm^{3+} concentration. Actually, as a result of the increase of Tm^{3+} content, the distance between Tm^{3+} becomes shorter. The interactions between neighboring Tm^{3+} ions get larger, which benefits the cross-relaxation (CR) process, $^1G_4$ + $^3H_6$→$^3F_{2,3}$ + $^3F_4$, as shown in Figure 3b. The CR process depopulates electrons in the $^1G_4$ level, while the electrons in $^3F_{2,3}$ and $^3F_4$ levels are populated via the CR process. Thus, blue emission intensities decrease quickly with the increase of Tm^{3+} even though the doping concentration is low. The NIR emission increases firstly and then decreases when the doping concentration is further increased due to the concentration quenching effect. Compared to a glass matrix, crystal exhibits a more compact structure. The distance between Tm^{3+} in GC is shorter than that in PG at the same doping concentration, resulting in the lower luminescence-quenching concentration in GC as compared to PG. The emission intensity at 802 nm reaches a maximum with the doping of 0.025 and 0.01Tm^{3+} in PG and GC, respectively. As shown in Figure 4b and the inset, the blue emissions around 450 and 480 nm in PG and GC both disappear and the UC spectra almost exhibit pure NIR emissions when the contents of Tm^{3+} exceed 0.01 mol%. A blue UC emission only being obtained in GC at a low doping concentration indicates most Tm^{3+} ions are incorporated into the KYb$_3$F$_{10}$ crystal structure with short interionic distance. The pure NIR emissions that are obtained at a very low doping concentration of Tm^{3+} indicates that the GC is an excellent candidate for pure NIR UC emission and is a significant UC luminescent material for promising applications in NIR fiber lasers and high-resolution biological imaging.
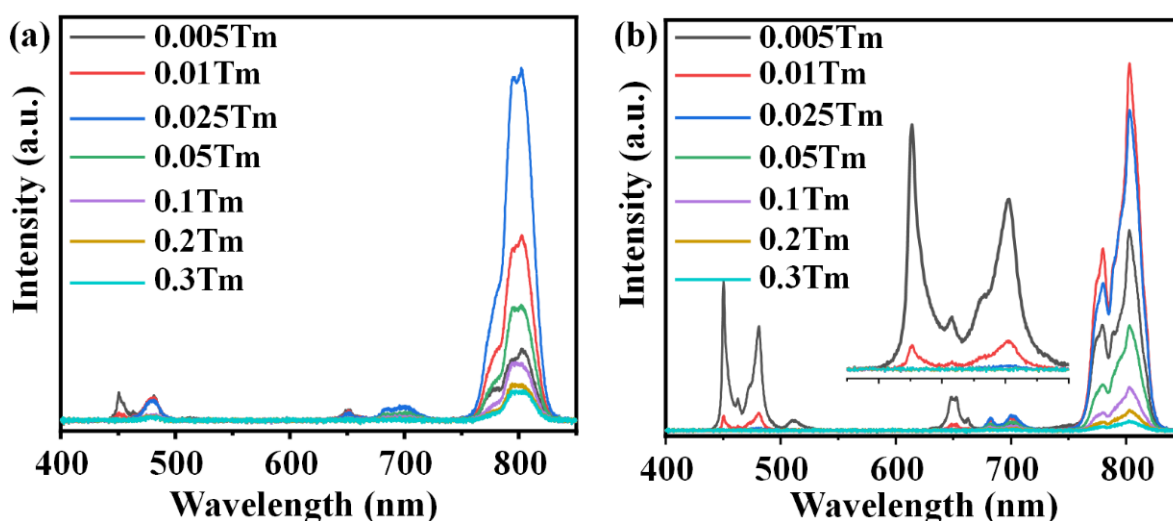

Figure 4. UC emission spectra of 1.0Yb^{3+}-yTm^{3+} co-doped (**a**) PG and (**b**) GC excited by a 980 nm LD. (y = 0.005~0.3).

As mentioned above, Yb^{3+} works as sensitizer ion for the UC emissions of Tm^{3+}. More importantly, Yb^{3+} also participates in the construction of fluoride nanocrystals and provides appropriate crystal sites for the incorporation of Tm^{3+}. The doping of Yb^{3+} plays a vital role in the precipitation of nanocrystals and enhancement of the UC emissions. The Yb^{3+}-concentration-dependent XRD patterns of the Yb^{3+}-Tm^{3+} co-doped and no-doped GCs are presented in Figure 5. It is found that only K$_2$SiF$_6$ crystals are precipitated in the

no-doped GC and these make no contribution to the enhancement of UC emission. Via the doping of Yb^{3+}, KYb_3F_{10} are precipitated in the GCs apart from K_2SiF_6 crystals as the Yb^{3+} content increases from 0.5 to 1.0 mol%. When Yb^{3+} concentration is set to 1.5 mol%, only the diffraction peaks of KYb_3F_{10} crystals are observed in the XRD pattern of GC. These results indicate that the precipitation of KYb_3F_{10} nanocrystals in the GCs is governed by the doping concentration of Yb^{3+} induced by Yb^{3+}. More interestingly, KYb_2F_7 crystals are also precipitated in the GCs when the Yb^{3+} concentration is increased from 2.0 to 3.5 mol%. In the XRD pattern of the $3.5Yb^{3+}$-$0.1Tm^{3+}$ co-doped sample, only the diffraction peaks of KYb_2F_7 crystals are observed. Therefore, the nano-crystallization in GC is induced by the doped Yb^{3+} and the crystalline phase in the GC can be controllably regulated from K_2SiF_6 to KYb_3F_{10} and further changes to KYb_2F_7 crystals by adjusting the concentration of Yb^{3+} from 0 to 3.5 mol%.
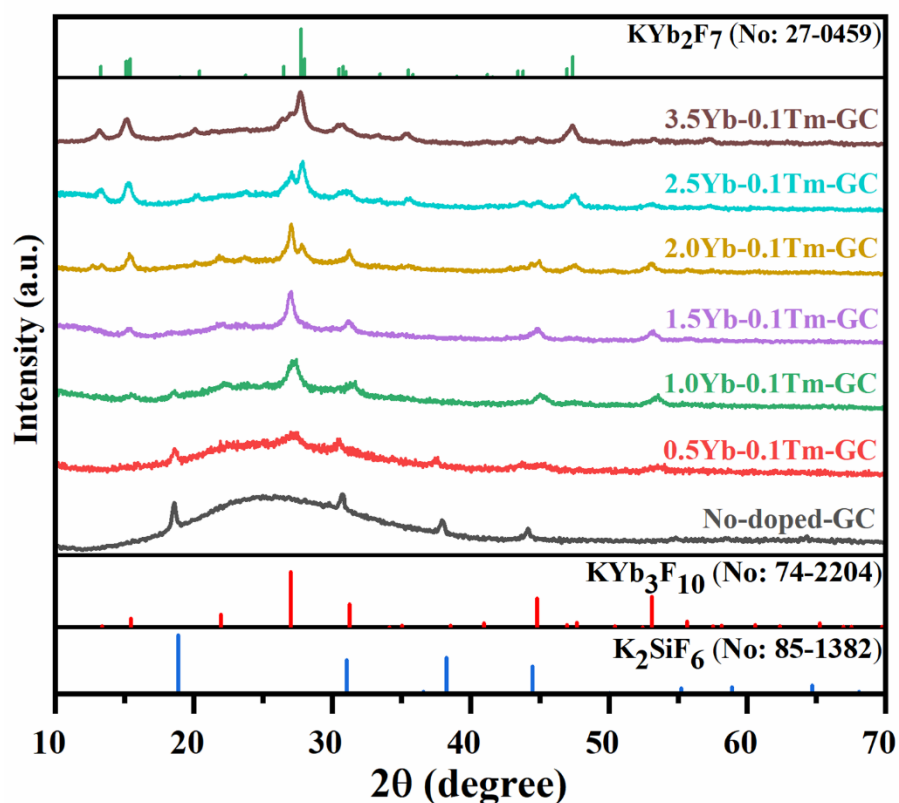
Figure 5. XRD patterns of xYb^{3+}-$0.1Tm^{3+}$ co-doped and no-doped GCs heat treated at 540 °C for 10 h. ($x = 0 \sim 3.5\%$).

Via the nano-crystallizations of KYb_3F_{10} and KYb_2F_7, Yb^{3+} ions are spontaneously confined within fluoride crystal structures. More importantly, Tm^{3+} can easily incorporate these two crystal structures by the substitution of Yb^{3+}. Owing to the extremely low phonon energies in the fluoride crystals, the probabilities of non-radiative transitions are low, which is beneficial for the efficient ET from Yb^{3+} to Tm^{3+} and enhanced UC emission of Tm^{3+}. The UC emission spectra of Yb^{3+}-Tm^{3+} co-doped GC with various concentrations of Yb^{3+} are shown in Figure 6a. Excited by a 980 nm LD, pure NIR UC emissions around 802 nm of Tm^{3+} are observed in the spectra of GCs. As the Yb^{3+} concentration increases from 0.5 to 1.5 mol%, the quantity of KYb_3F_{10} nanocrystals precipitated in the GCs is increased, and the amount of Tm^{3+} and Yb^{3+} ions located in the fluoride crystal structures are increased. The emission intensity enhances firstly, reaching a maximum at 1.0 mol% Yb^{3+}, and then decreases when the Yb^{3+} concentration is increased to 1.5 mol% due to the concentration quenching effect caused by the severe interactions between Ln^{3+} ions. When the Yb^{3+} concentration is further increased to 2.0 mol%, KYb_2F_7 crystals start to precipitate

in the GCs. A part of the Tm^{3+} enter KYb_2F_7 nanocrystals in the $2.0Yb^{3+}$-$0.1Tm^{3+}$ co-doped GC, which disperses the distribution of Tm^{3+} and increases the NIR UC emission intensity again. When the Yb^{3+} concentration increases from 2.0 to 3.5 mol%, more KYb_2F_7 crystals are precipitated in the GCs, more Tm^{3+} ions are incorporated into KYb_2F_7 crystals, and the UC emission intensity at 800 is increased monotonically. It is also found that the profile of the emission spectrum for the 3.5 Yb^{3+}-$0.1Tm^{3+}$ co-doped GCs is different from that of the $1.0Yb^{3+}0.1Tm^{3+}$ co-doped samples (inset of Figure 6a), which in turn proves that Tm^{3+} are incorporated in two different crystal environments in the two GCs containing different nanocrystals. Compared to KYb_2F_7 crystal, more Yb^{3+} ions are distributed in the crystal structure in KYb_3F_{10}. The luminescent-quenching concentration of the UC emission in KYb_2F_7 crystal is higher than that in KYb_3F_{10}. The emission intensity in $3.5Yb^{3+}$-$0.1Tm^{3+}$ co-doped GC is 7 times higher than that in the $1.0Yb^{3+}$-$0.1Tm^{3+}$ sample, which indicates that the nano-crystallization of KYb_2F_7 provides more excellent crystal environments for achieving more efficient NIR UC emission of Tm^{3+}.
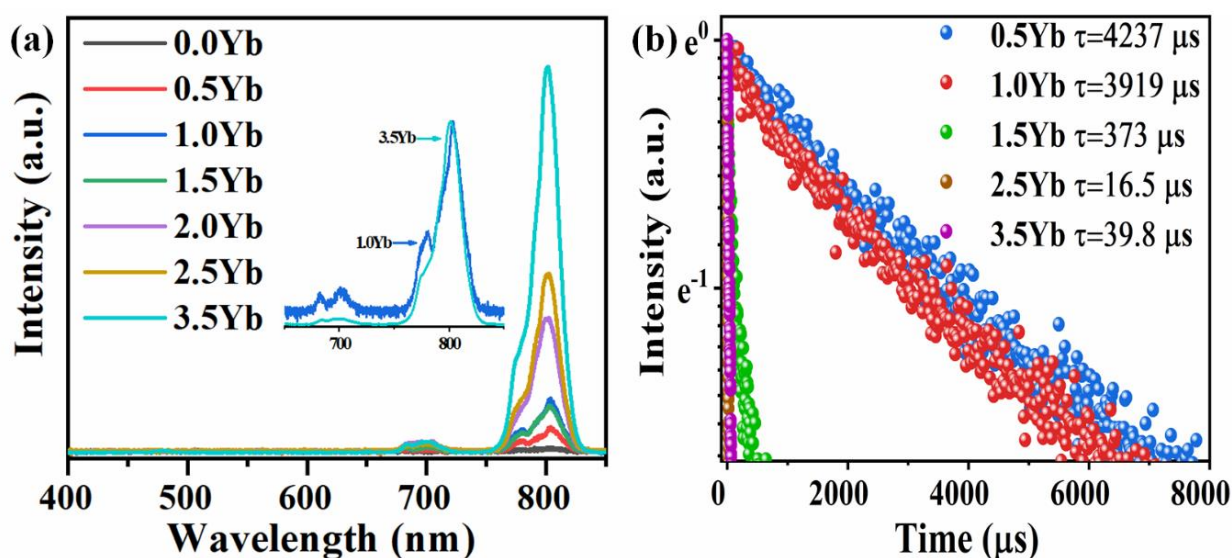
Figure 6. (**a**) UC emission spectra xYb^{3+}-0.1Tm^{3+}co-doped GCs heat treated at 540 °C for 5 h. (x = 0.0~3.5). (**b**) Emission decay curves of xYb^{3+}-0.1Tm^{3+} co-doped PG and GCs heat treated at 540 °C for 5 h monitored at 802 nm emission. (x = 0.5~3.5).

The UC emission decay curves of the Yb^{3+}-Tm^{3+} co-doped GCs monitored at 802 nm are shown in Figure 6b. The lifetime of the NIR emission decreases as Yb^{3+} concentration increases from 0.5 to 1.5 mol%. Especially, the lifetime of the $1.5Yb^{3+}$-$0.1Tm^{3+}$ co-doped GC decreases dramatically to 373 μs due to the severe interaction between the neighboring Tm^{3+} in KYb_3F_{10} crystals. However, the lifetime increases from 16.5 to 39.8 μs when the Yb^{3+} concentration is increased from 2.5 to 3.5 mol%. These results also prove that the coordinated environments of Tm^{3+} in high-doping GCs (2.5 and 3.5 mol% Yb^{3+}-$0.1Tm^{3+}$) is distinct to that in low-doping GCs (0.5, 1.0, and 1.5 mol% Yb^{3+}-$0.1Tm^{3+}$). Therefore, the precipitation of KYb_2F_7 nanocrystals in GCs further enhances the NIR UC emission of Tm^{3+} and provides a significant matrix for applications in photonic devices, in particular of high-efficiency UC fiber lasers.

4. Conclusions

In summary, transparent Yb^{3+}-Tm^{3+} co-doped GCs were prepared in this work for greatly enhancing the UC luminescence of Tm^{3+}. The GCs possessed high transmittance (>85.0%) though fluoride nanocrystals were precipitated among the glass matrices. K_2SiF_6 crystals are precipitated in the no-doped GC. However, KYb_3F_{10} and KYb_2F_7 nanocrystals were controllably and successively precipitated in the GCs via the inducing of Yb^{3+} when

the doping concentration of Yb^{3+} changed from 0.5 to 3.5 mol%. UC emissions of Tm^{3+} were dramatically enhanced when Ln^{3+} ions were incorporated into KYb_3F_{10} crystal structures as the Yb^{3+} concentration changed from 0.5 to 1.5 mol%. Pure NIR UC emissions were obtained by adjusting the concentration of Tm^{3+}. KYb_2F_7 nanocrystals were precipitated in GCs when the Yb^{3+} concentration exceeded 2.0 mol%. More efficient UC emissions were achieved via the precipitation of KYb_2F_7 than that of KYb_3F_{10} in GCs. The designed GCs offer potential optical gain materials for highly-efficient NIR UC photoluminescence. More importantly, the Yb^{3+}-induced nano-crystallization strategy paves a new way for the design and fabrication of emerging GCs to provide excellent crystal environments for Ln^{3+}.

Author Contributions: Conceptualization, Z.F. and J.L.; methodology, J.L.; Y.L. and Q.Z.; formal analysis, J.L.; Y.L.; Q.Z. and S.Z.; investigation, J.L.; Y.L.; Q.Z. and Z.F.; resources, S.Z.; Z.F. and B.-O.G.; data curation, J.L.; Y.L.; Q.Z. and Z.F.; writing-original draft, J.L.; writing-review and editing, S.Z.; Z.F. and B.-O.G.; supervision, Z.F. and B.-O.G.; project administration, Z.F. and B.-O.G.; funding acquisition, Z.F.; S.Z. and B.-O.G. All authors have read and agreed to the published version of the manuscript.

Conflicts of Interest: The authors declare no conflict of interest.

References

1. Zhou, J.; Gu, F.; Liu, X.; Qiu, J. Enhanced multiphoton upconversion in single nanowires by waveguiding excitation. *Adv. Opt. Mater.* **2016**, *4*, 1174–1178. [CrossRef]
2. Zhou, J.; Leano, J.L., Jr.; Liu, Z.; Jin, D.; Wong, K.L.; Liu, R.S.; Bunzli, J.G. Impact of lanthanide nanomaterials on photonic devices and smart applications. *Small* **2018**, *14*, e1801882. [CrossRef]
3. Wen, S.; Zhou, J.; Zheng, K.; Bednarkiewicz, A.; Liu, X.; Jin, D. Advances in highly doped upconversion nanoparticles. *Nat. Commun.* **2018**, *9*, 2415. [CrossRef] [PubMed]
4. Wang, F.; Han, Y.; Lim, C.S.; Lu, Y.; Wang, J.; Xu, J.; Chen, H.; Zhang, C.; Hong, M.; Liu, X. Simultaneous phase and size control of upconversion nanocrystals through lanthanide doping. *Nature* **2010**, *463*, 1061–1065. [CrossRef]
5. Wang, F.; Wang, J.; Liu, X. Direct evidence of a surface quenching effect on size-dependent luminescence of upconversion nanoparticles. *Angew. Chem. Int. Ed. Engl.* **2010**, *49*, 7456–7460. [CrossRef] [PubMed]
6. Wang, J.; Deng, R.; MacDonald, M.A.; Chen, B.; Yuan, J.; Wang, F.; Chi, D.; Hor, T.S.; Zhang, P.; Liu, G.; et al. Enhancing multiphoton upconversion through energy clustering at sublattice level. *Nat. Mater.* **2014**, *13*, 157–162. [CrossRef]
7. Wang, J.; Wang, F.; Wang, C.; Liu, Z.; Liu, X. Single-band upconversion emission in lanthanide-doped $KMnF_3$ nanocrystals. *Angew. Chem. Int. Ed. Engl.* **2011**, *50*, 10369–10372. [CrossRef]
8. Zhou, B.; Shi, B.; Jin, D.; Liu, X. Controlling upconversion nanocrystals for emerging applications. *Nat. Nanotechnol.* **2015**, *10*, 924–936. [CrossRef]
9. Auzel, F. Upconversion and Anti-Stokes Processes with f and d Ions in Solids. *Chem. Rev.* **2004**, *104*, 139–174. [CrossRef]
10. Chen, G.Y.; Ohulchanskyy, T.Y.; Kumar, R.; Agren, H.; Prasad, P.N. Ultrasmall monodisperse $NaYF_4$:Yb^{3+}/Tm^{3+} nanocrystals with enhanced Near-Infrared to Near-Infrared upconversion photoluminescence. *Acs Nano* **2010**, *4*, 3163–3168. [CrossRef]
11. Fernandez-Bravo, A.; Yao, K.; Barnard, E.S.; Borys, N.J.; Levy, E.S.; Tian, B.; Tajon, C.A.; Moretti, L.; Altoe, M.V.; Aloni, S.; et al. Continuous-wave upconverting nanoparticle microlasers. *Nat. Nanotechnol.* **2018**, *13*, 572–577. [CrossRef]
12. Liu, Q.; Sun, Y.; Yang, T.; Feng, W.; Li, C.; Li, F. Sub-10 nm hexagonal lanthanide-doped $NaLuF_4$ upconversion nanocrystals for sensitive bioimaging in vivo. *J. Am. Chem. Soc.* **2011**, *133*, 17122–17125. [CrossRef] [PubMed]
13. Zhang, W.J.; Zhang, J.P.; Wang, Z.; Wang, W.C.; Zhang, Q.Y. Spectroscopic and structural characterization of transparent fluorogermanate glass ceramics with LaF_3:Tm^{3+} nanocrystals for optical amplifications. *J. Alloys Compd.* **2015**, *634*, 122–129. [CrossRef]
14. Chen, G.; Lei, R.; Huang, F.; Wang, H.; Zhao, S.; Xu, S. Effects of Tm^{3+} concentration on upconversion luminescence and temperature-sensing behavior in Tm^{3+}/Yb^{3+}:Y_2O_3 nanocrystals. *J. Biolumin. Chemilumin.* **2018**, *33*, 1262–1267.
15. Chen, S.; Song, W.; Cao, J.; Hu, F.; Guo, H. Highly sensitive optical thermometer based on FIR technique of transparent NaY_2F_7:Tm^{3+}/Yb^{3+} glass ceramic. *J. Alloys Compd.* **2020**, *825*, 154011. [CrossRef]
16. Li, X.; Yang, C.; Yu, Y.; Li, Z.; Lin, J.; Guan, X.; Zheng, Z.; Chen, D. Dual-modal photon upconverting and downshifting emissions from ultra-stable $CsPbBr_3$ perovskite nanocrystals triggered by co-growth of Tm:$NaYbF_4$ nanocrystals in glass. *ACS Appl Mater. Interfaces* **2020**, *12*, 18705–18714. [CrossRef] [PubMed]

17. Liu, Y.; Lu, Y.; Yang, X.; Zheng, X.; Wen, S.; Wang, F.; Vidal, X.; Zhao, J.; Liu, D.; Zhou, Z.; et al. Amplified stimulated emission in upconversion nanoparticles for super-resolution nanoscopy. *Nature* **2017**, *543*, 229–233. [CrossRef]

18. Xiang, S.; Zheng, H.; Zhang, Y.; Peng, T.; Zhang, X.; Chen, B. Effect of Tm^{3+} concentration and temperature on blue and NIR upconversion luminescence in Tm^{3+}/Yb^{3+} co-doped $NaY(WO_4)_2$ microstructures. *J. Nanosci. Nanotechnol.* **2016**, *16*, 636–642. [CrossRef]

19. Xu, W.; Gao, X.; Zheng, L.; Zhang, Z.; Cao, W. An optical temperature sensor based on the upconversion luminescence from Tm^{3+}/Yb^{3+} codoped oxyfluoride glass ceramic. *Sens. Actuators B* **2012**, *173*, 250–253. [CrossRef]

20. Zhou, J.; Chen, G.; Zhu, Y.; Huo, L.; Mao, W.; Zou, D.; Sun, X.; Wu, E.; Zeng, H.; Zhang, J.; et al. Intense multiphoton upconversion of Yb^{3+}-Tm^{3+} doped β-$NaYF_4$ individual nanocrystals by saturation excitation. *J. Mater. Chem. C* **2015**, *3*, 364–369. [CrossRef]

21. Zhang, C.; Zhang, J.; Lin, C.; Dai, S.; Chen, F. Improvement of third-order nonlinear properties in GeS_2-Sb_2S_3-$CsCl$ chalcogenide glass ceramics embedded with CsCl nano-crystals. *Ceram. Int.* **2020**, *46*, 27990–27995. [CrossRef]

22. Velázquez, J.; Gorni, G.; Balda, R.; Fernández, J.; Pascual, L.; Durán, A.; Pascual, M. Non-linear optical properties of Er^{3+}-Yb^{3+}-doped $NaGdF_4$ nanostructured glass-ceramics. *Nanomaterials* **2020**, *10*, 1425. [CrossRef] [PubMed]

23. Cai, M.; Wei, T.; Zhou, B.; Tian, Y.; Zhou, J.; Xu, S.; Zhang, J. Analysis of energy transfer process based emission spectra of erbium doped germanate glasses for mid-infrared laser materials. *J. Alloys Compd.* **2015**, *626*, 165–172. [CrossRef]

24. Chen, Y.; Liu, J.; Zhao, N.; Zhang, W.; Zhu, M.; Zhou, G.; Hou, Z. Manufacture and spectroscopic analysis of Tm^{3+}-doped silica glass and microstructure optical fiber through the laser sintering technique. *Appl. Phys. Express* **2019**, *12*, 122012. [CrossRef]

25. Mi, C.; Zhou, J.; Wang, F.; Lin, G.; Jin, D. Ultrasensitive ratiometric nanothermometer with large dynamic range and photostability. *Chem. Mater.* **2019**, *31*, 9480–9487. [CrossRef]

26. Zhan, Q.Q.; Qian, J.; Liang, H.J.; Somesfalean, G.; Wang, D.; He, S.L.; Zhang, Z.G.; Andersson-Engels, S. Using 915 nm laser excited $Tm^{3+}/Er^{3+}/Ho^{3+}$-Doped $NaYbF_4$ upconversion nanoparticles for in vitro and deeper in vivo bioimaging without overheating irradiation. *ACS Nano* **2011**, *5*, 3744–3757. [CrossRef] [PubMed]

27. Li, X.; Chen, D.; Huang, F.; Chang, G.; Zhao, J.; Qiao, X.; Xu, X.; Du, J.; Yin, M. Phase-Selective nanocrystallization of $NaLnF_4$ in aluminosilicate glass for random laser and 940 nm LED-excitable upconverted luminescence. *Laser Photonics Rev.* **2018**, *12*, 1800030. [CrossRef]

28. Gorni, G.; Velázquez, J.; Mosa, J.; Mather, G.; Serrano, A.; Vila, M.; Castro, G.; Bravo, D.; Balda, R.; Fernández, J.; et al. Transparent sol-gel oxyfluoride glass-ceramics with high crystalline fraction and study of re incorporation. *Nanomaterials* **2019**, *9*, 530. [CrossRef]

29. Yanes, A.C.; Santana-Alonso, A.; Méndez-Ramos, J.; del-Castillo, J.; Rodríguez, V.D. Novel sol-gel nano-glass-ceramics comprising Ln^{3+}-doped YF_3 nanocrystals: Structure and high efficient UV up-conversion. *Adv. Funct. Mater.* **2011**, *21*, 3136–3142. [CrossRef]

30. Chen, D.; Peng, Y.; Li, X.; Zhong, J.; Huang, H.; Chen, J. Simultaneous tailoring of dual-phase fluoride precipitation and dopant distribution in glass to control upconverting luminescence. *ACS Appl. Mater. Interfaces* **2019**, *11*, 30053–30064. [CrossRef]

31. Walas, M.; Lewandowski, T.; Synak, A.; Łapiński, M.; Sadowski, W.; Kościelska, B. Eu^{3+} doped tellurite glass ceramics containing SrF_2 nanocrystals: Preparation, structure and luminescence properties. *J. Alloys Compd.* **2017**, *696*, 619–626. [CrossRef]

32. Chen, D.; Peng, Y.; Li, X.; Zhong, J.; Huang, P. Competitive nanocrystallization of Na_3ScF_6 and $NaYbF_4$ in aluminosilicate glass and optical spectroscopy of Ln^{3+} dopants. *Ceram. Int.* **2018**, *44*, 15666–15673. [CrossRef]

33. Fang, Z.; Chen, Z.; Peng, W.; Shao, C.; Zheng, S.; Hu, L.; Qiu, J.; Guan, B.O. Phase-separation engineering of glass for drastic enhancement of upconversion luminescence. *Adv. Opt. Mater.* **2019**, *7*, 1801572. [CrossRef]

34. Zhou, J.; Chen, G.; Wu, E.; Bi, G.; Wu, B.; Teng, Y.; Zhou, S.; Qiu, J. Ultrasensitive polarized up-conversion of Tm^{3+}-Yb^{3+} doped beta-$NaYF_4$ single nanorod. *Nano Lett.* **2013**, *13*, 2241–2246. [CrossRef] [PubMed]

35. Zhou, J.; Wen, S.; Liao, J.; Clarke, C.; Tawfik, S.A.; Ren, W.; Mi, C.; Wang, F.; Jin, D. Activation of the surface dark-layer to enhance upconversion in a thermal field. *Nat. Photonics* **2018**, *12*, 154–158. [CrossRef]

36. Gao, G.; Busko, D.; Joseph, R.; Howard, I.A.; Turshatov, A.; Richards, B.S. Highly efficient La_2O_3:Yb^{3+},Tm^{3+} single-band NIR-to-NIR upconverting microcrystals for anti-counterfeiting applications. *ACS Appl. Mater. Interfaces* **2018**, *10*, 39851–39859. [CrossRef]

37. Su, J.-Y.; Zhang, X.-Y.; Li, X.; Qu, M.-L. Synthesis and luminescence properties of Yb^{3+}, Tm^{3+} and Ho^{3+} co-doped $SrGd_2(WO_4)_2(MoO_4)_2$ nano-crystal. *Adv. Powder Technol.* **2020**, *31*, 1051–1059. [CrossRef]

38. Arppe, R.; Hyppanen, I.; Perala, N.; Peltomaa, R.; Kaiser, M.; Wurth, C.; Christ, S.; Resch-Genger, U.; Schaferling, M.; Soukka, T. Quenching of the upconversion luminescence of $NaYF_4$:Yb^{3+}, Er^{3+} and $NaYF_4$:Yb^{3+}, Tm^{3+} nanophosphors by water: The role of the sensitizer Yb^{3+} in non-radiative relaxation. *Nanoscale* **2015**, *7*, 11746–11757. [CrossRef] [PubMed]

39. Fu, Y.; Zhao, L.; Guo, Y.; Yu, H. Highly sensitive optical thermometers based on unconventional thermometric coupled levels of Tm^{3+} following a Boltzmann-type distribution in oxyfluoride glass ceramics. *New J. Chem.* **2019**, *43*, 16664–16669. [CrossRef]

40. Zhao, J.; Jin, D.; Schartner, E.P.; Lu, Y.; Liu, Y.; Zvyagin, A.V.; Zhang, L.; Dawes, J.M.; Xi, P.; Piper, J.A.; et al. Single-nanocrystal sensitivity achieved by enhanced upconversion luminescence. *Nat. Nanotechnol.* **2013**, *8*, 729–734. [CrossRef]

41. Fu, Y.; Zhao, L.; Guo, Y.; Wu, B.; Dong, H.; Yu, H. Ultrapure NIR-to-NIR single band emission of β-PbF_2: Yb^{3+}/Tm^{3+} in glass ceramics. *J. Lumin.* **2019**, *208*, 33–38. [CrossRef]

42. Fu, Y.; Zhao, L.; Guo, Y.; Yu, H. Up-conversion luminescence lifetime thermometry based on the $^1G_4$ state of Tm^{3+} modulated by cross relaxation processes. *Dalton Trans.* **2019**, *48*, 16034–16040. [CrossRef] [PubMed]